ARTICLE

Liquid-phase catalytic growth of graphene

Pin Tian,[a,b,c] Libin Tang,[*b,c] Jinzhong Xiang,[*a] Shu Ping Lau,[d] Shouzhang Yuan,[b,c] Dengquan Yang,[b] Lain-Jong Li[e] and Kar Seng Teng[*f]

Received 00th January 20xx,
Accepted 00th January 20xx

DOI: 10.1039/x0xx00000x

Ability to mass produce graphene at low cost is of paramount importance in bringing graphene based technologies into market. Here we report a facile liquid-phase catalytic growth of graphene suitable for mass production. Iodine tincture is used to catalyze graphene quantum dots to form graphene films at room temperature. Such method has many advantages, such as environment friendly, high yield, low cost and wide choice of substrates. Furthermore, bandgap of the graphene films is tunable by post-annealing. A photodetector based on the graphene films was developed and could response to a broad wavelength between 365 and 1200 nm. It exhibited detectivity and responsivity of up to 1.1 x 10^{13} cmHz$^{1/2}$W^{-1} and 81.3 mAW^{-1}, respectively. Hence, the graphene films demonstrated significant applications in the field of optoelectronics. Interestingly, surface of the graphene film prepared by this method has wrinkles that can also be explored for energy storage applications.

Introduction

Graphene, a pioneer of two-dimensional materials, has attracted great scientific interests due to its excellent physical and chemical properties since its discovery by Andre Geim's group.[1] An extensive research on the properties of the material has led to many novel applications, such as flexible devices,[2-6] transparent electrodes,[7-13] ultra-fast photodetectors[14-17] and wearable temperature sensors[18-20] by taking advantage of graphene's high transmittance (e.g. visible light transmittance of 97.7%[21]), flexibility, conductivity (e.g. high carrier mobility of 2.5x10^5 cm^{2}V^{-1}s^{-1}[22] at room temperature) and thermal conductivity (of 3000 WmK^{-1}[23]). Also, the magnetic property of graphene has led to the development of unique filter membrane.[24,25] Other applications include high performance energy storage[26-30] by utilizing the surface wrinkles of graphene. Although there are many reports on the novel applications of graphene, most of these developments remain in research laboratories and have not reached the mass market due to inability to mass produce graphene at low cost. Therefore, there is an urgent need to develop a preparation technique that is suitable for low cost mass production of graphene in order to bring graphene based technologies to the mass market. At present, there are several mainstream techniques to produce graphene, such as mechanical stripping method,[31,32] chemical vapour deposition methods,[33-36] epitaxial growth methods,[37-39] liquid stripping methods or redox methods,[40-42] and molecular self-assembly methods.[43-46] Each of these methods has advantages and disadvantages, for example, graphene prepared by mechanical stripping exhibits the best material quality and device performances however this method is only suitable for laboratory research due to its low yield. The conventional metal-catalyzed chemical vapour deposition method is also extremely low in yield due to the complex preparation processes, especially the transfer process. More recently, various chemical vapour deposition methods have been developed, such as metal-catalyst-free chemical vapour deposition[47] and plasma enhanced chemical vapour deposition,[48,49] to avoid detrimental defects caused by the transfer process in the conventional metal-catalyzed chemical vapour deposition methods. However, graphene produced by these methods exhibits significantly reduced performances due to imperfect nucleation and absence of catalytic reaction. The current solution based processing techniques, such as liquid-phase stripping and redox methods, can produce graphene films easily and at very high yield, but they require the use of strong acids and alkali as well as highly toxic and explosive chemicals, which are very harmful to the environment. Hence, these methods are unsuitable for industrial production of graphene for environmental reasons. The molecular self-assembly method is considered current state of the art technology due to facile, high-yield and scalable synthesis process[50] but it is limited by the choice of precursors that are required to meet a series of thermodynamic, kinetic, and structural criteria imposed by the dimensions and symmetry, the nature of the surface used as growth substrate, and technical limitations imposed by the UHV system used in fabrication,[51] hence resulting in high production cost of graphene.

Here we developed a facile liquid-phase catalysis method to produce graphene. Fig. 1a illustrates the entire process. Firstly, graphene quantum dots (GQDs) are prepared using sucrose as

[a.] School of Physics and Astronomy, Yunnan University, Kunming 650091, P.R. China.
[b.] Kunming Institute of Physics, Kunming 650223, P.R. China.
[c.] Yunnan Key Laboratory of Advanced Photoelectric Materials & Devices, Kunming 650223, P.R. China.
[d.] Department of Applied Physics, The Hong Kong Polytechnic University, Hong Kong SAP, P.R. China.
[e.] School of Materials Science and Engineering, University of New South Wales, Sydney 2052, Australia.
[f.] Department of Electronic and Electrical Engineering, Swansea University, Bay Campus, Fabian Way, Swansea SA1 8EN, United Kingdom.
† These authors contributed equally.
Electronic Supplementary Information (ESI) available: [details of any supplementary information available should be included here]. See DOI: 10.1039/x0xx00000x

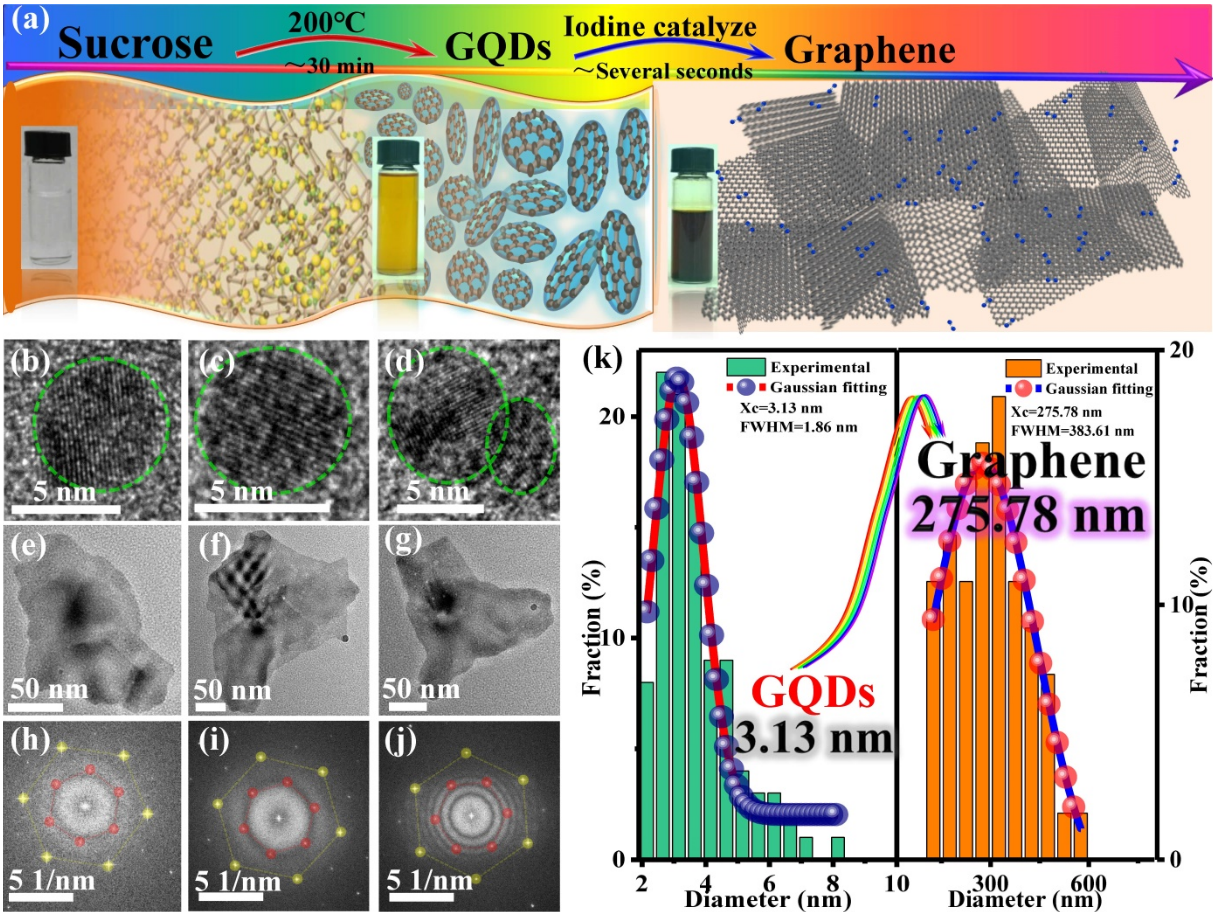

Fig. 1 Liquid-phase catalytic growth of graphene and TEM characterization. (a) Schematic diagram illustrating the liquid-phase catalytic growth process of graphene. Sucrose solution (left) was annealed at 200℃ and turned from colorless to yellow solution (after 30 min), which consisted of solution containing GQDs (middle). Iodine, acting as catalyst (represented as blue molecules in the diagram on the right), was added in to the GQDs solution and turned the solution into dark brown (right) (after several seconds), which consisted of the liquid-phase catalyzed graphene. (b-d) High resolution TEM image of GQDs. (e-j) TEM image of graphene flakes produced by the liquid-phase catalytic method. (h-j) Fast Fourier transform (FFT) patterns of (e), (f) and (g), respectively. (k) Size distribution of the GQDs (left) and graphene (right) prepared by the liquid-phase catalysis method. The statistical size of GQDs and graphene are 3.13 nm and 275.78 nm, respectively.

precursor. They are then catalyzed into graphene films using iodine as catalyst. Unlike conventional catalyst-based chemical vapour deposition method that requires elevated temperature to prepare graphene films,[52] the liquid-phase catalysis method using iodine as catalyst can rapidly produce graphene at ambient temperature. Hence, this method has many advantages, such as environment friendly, low cost, high yield, simple and rapid preparation process, low energy consumption, and wide choice of substrates. Importantly, this method is highly suitable for mass production of graphene at low cost, which will expedite the commercialization of graphene based technologies. Furthermore, the method might stimulate ideas for low-cost mass production of other 2D materials. In this work, a photodetector was developed using graphene films prepared by the liquid-phase catalysis method. Characterization of the device suggests that the absorption layer at the photodetector was formed by multilayer graphene stacking. This is different from the orderly stacking graphite, which cannot be used in optoelectronic devices due to coupling of interlayer charge. The photodetector could response to a broad wavelength range between 365 and 1200 nm, with detectivity (D^*) of up to $1.1\text{x}10^{13}$ $\text{cmHz}^{1/2}\text{W}^{-1}$ and responsivity of up to 81.3 mAW^{-1}. Therefore, these graphene films prepared by the liquid-phase catalysis method can find applications in the field of optoelectronics, such as photodetectors, solar cells and light-emitting diodes, as well as in other fields, such as energy storage, due to their interesting surface morphology.

Results and discussion

Fig. 1a shows a schematic diagram of the liquid-phase catalytic growth process of graphene. Colorless sucrose solution was caramelized at 200℃ to form GQDs, which turned the solution into a yellow viscous liquid. Subsequently, the viscous liquid was diluted with a mixed solvent of alcohol and deionized water. Iodine was then introduced into the GQDs solution and turned the color of the solution from yellow to dark brown, as shown in right inset of Fig. 1(a). Details on the preparation process can be found in experimental section. TEM characterization on the yellow solution showed high density and even distribution of GQDs, as shown in Fig. S1(a) and (b), ESI†. The size of these quantum dots was 3.13 nm as shown in Fig. 1(k). High-resolution TEM (HRTEM) image in Fig. 1(b-d) revealed circular shape of the as-grown GQDs. Fig. S2(a) and (b), ESI† show the lattice fringes of the dots with spacing of 0.214 nm and 0.246 nm respectively, which is characteristic spacing of graphene. After the introduction of iodine, the GQDs rapidly grew in size from a few nanometers to hundreds of nanometers and into graphene flakes as shown in HRTEM image of Fig. 1(e-g). Interestingly, there were wrinkles at the graphene prepared by the liquid-phase catalysis method as shown in Fig. S1(d), ESI†. Lattice fringes from region ① and ② of the HRTEM image in Fig. S1d , ESI†are shown in Fig. S2(c) and (d), ESI†, which has lattice spacing of 0.214 nm in-plane and 0.361 nm in c-axial direction respectively. This revealed good crystallinity of graphene. Selective area electron diffraction (SAED) was performed at the blue dotted circle region in Fig. S1(c), ESI†, which showed hexagonal diffraction pattern of graphene (Fig. S2(e), ESI†). Furthermore, the FFT patterns of Fig. 1(e-g) showed perfect hexagonal structures, as shown in Fig. 1(h-j) respectively. Hence, these results again indicated good crystallinity of graphene prepared by this method. Interestingly, the statistical size of graphene flakes was up to 275.78 nm, as shown in Fig. 1(k). There were evidences that the size of some graphene flakes could reach micron scale as shown in Fig. 2(a). This implies that the liquid-phase catalysis method is capable of mass producing graphene with size ranging from hundreds of nanometers to micron scale. Further characterizations revealed high quality of the graphene film produced by this method as shown in Fig. S7. EDS measurements (Fig. S1(e), ESI†) showed

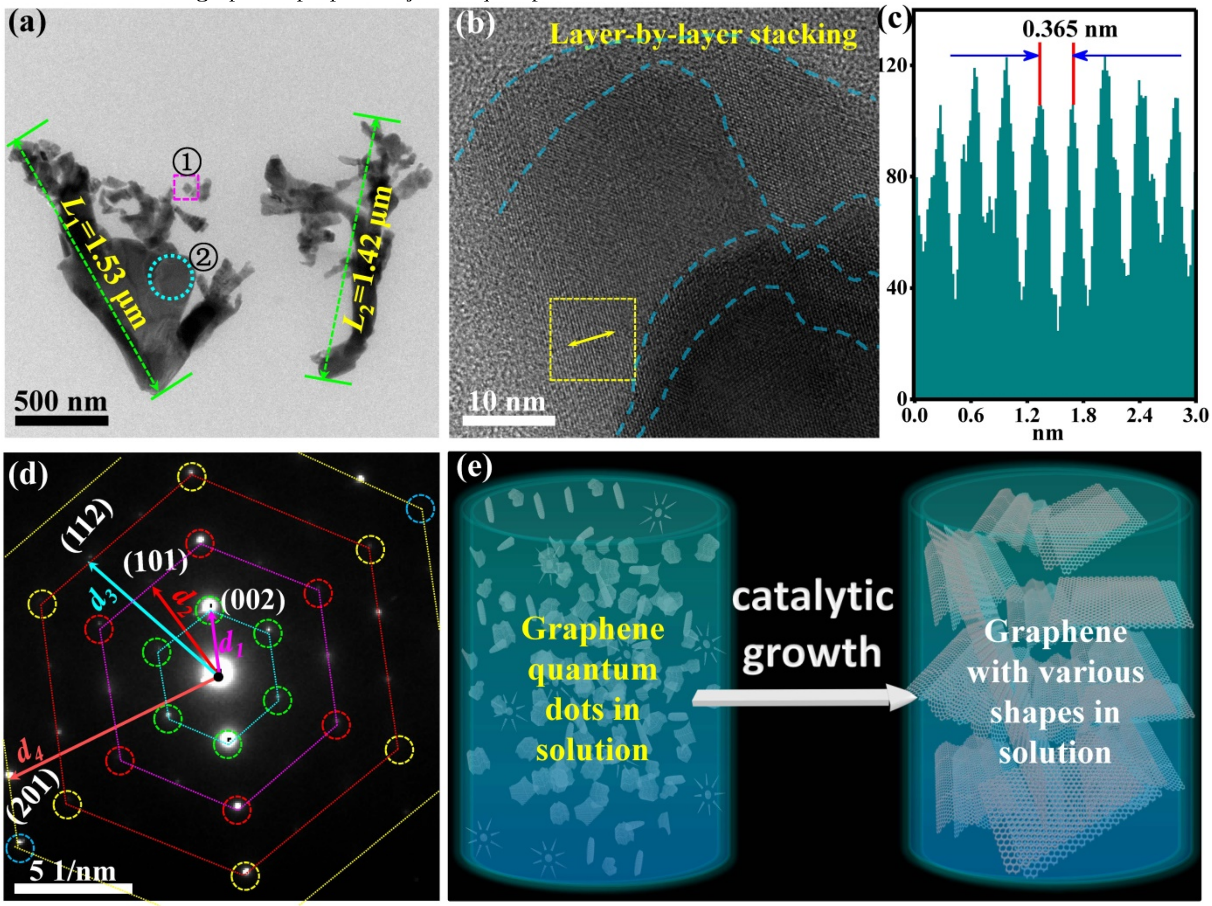

Fig. 2 Structural and elemental characterization of graphene prepared by liquid-phase catalytic method. (a) TEM image of liquid-phase catalytic graphene with size of up to micron scale. (b) High-resolution TEM image of region ① in Fig. 2(a). It revealed the layer-by-layer stacking structure of the liquid-catalyzed graphene. The blue dotted area in the image shows the intricate stacking of graphene. (c) Line profile of the yellow rectangular region in Fig. 2(b). An interlayer spacing of 0.365 nm was observed at the layered structure. (d) Selected area electron diffraction (SAED) pattern of region ② in Fig. 2(a). d_1, d_2, d_3 and d_4 are the distances between the center point and the hexagonal vertex of electron diffraction, which indicate the lattice faces of several vertices, such as (002), (101) , (112) and (201), respectively. (e) Schematic diagram illustrating the growth of graphene from GQDs solution catalyzed using iodine to form various morphologies of graphene flakes via the liquid-phase catalytic growth method.

high concentration of iodine element on the graphene, suggesting that the iodine remained in the solution and attached to the graphene after completion of the catalytic growth. Fig. 2(b) shows a HRTEM image of region ① in Fig. 2(a). It showed that multi-layered graphene was produced in the solution using the liquid-phase catalysis method. Besides, the interlayer spacing of 0.365 nm, as measured in Fig. 2(c), indicates that the graphene produced using this method is constructed by layer-by-layer stacking. SAED were performed (as shown in Fig. 2(d)) to investigate the superposition of the graphene. By measuring the distance (d) between the center spot and the vertices of each hexagonal ring, D (e.g. $D = 1/d$) of each lattice face can be calculated. According to the crystal surface spacing of graphite, the corresponding lattice face of each spot was obtained, as shown in Fig. 2(d), where d_1=2.946 1/nm, d_2=4.950 1/nm, d_3=8.620 1/nm and d_4=9.481 1/nm corresponding to D_1=0.339 nm, D_2=0.202 nm, D_3=0.116 nm and D_4=0.105 nm respectively. Thus, the electron diffraction pattern corresponded to the lattice face[53] (002), (101), (112) and (201), which indicate c-axis direction as well as other directions of graphene. This suggests that the graphene flakes were randomly stacked. Also, the TEM images showed that the graphene flakes were not flat but have lots of wrinkles. Therefore, graphene with various morphologies can be grown from GQDs using this method, as illustrated in Fig. 2(e).

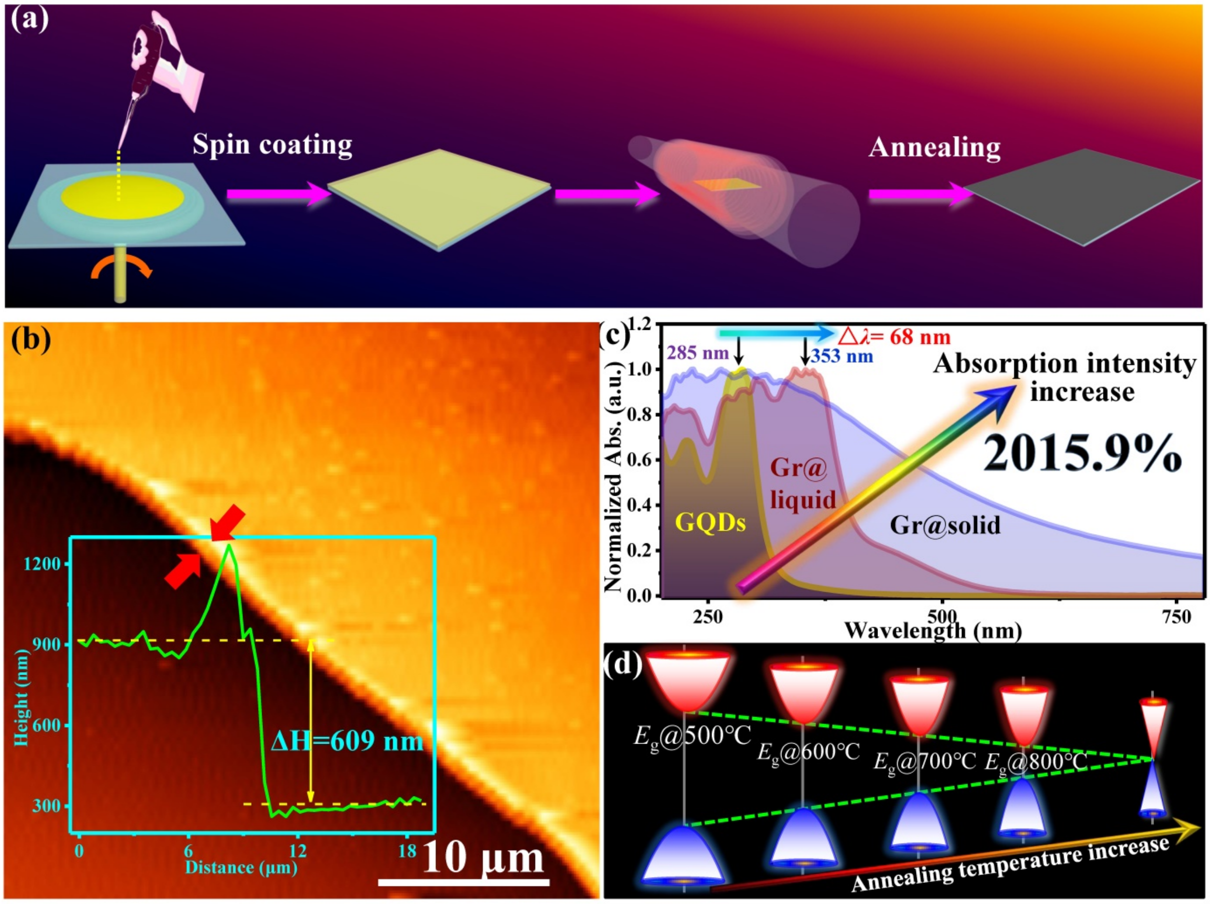

Fig. 3 Preparation and characterization of solid graphene film, and its energy gap modulation. (a) Schematic diagram on the preparation process of solid graphene films. (b) AFM image of solid graphene films. Inset shows line profile taken across the red arrows. The measured thickness of the film was 609 nm. (c) Normalized UV-visible-infrared spectroscopy measurements of GQDs, liquid graphene solution (Gr@liquid) and solid graphene films (Gr@solid). Red-shift of 68 nm in the absorption peaks of GQDs (285 nm) was observed after catalyzed to form graphene (353 nm). Intensity of absorption was increased by 2015.9% from the GQDs and after the liquid graphene was spin-coated and annealed to form solid graphene film. Further widening of the absorption spectrum was observed on the graphene film. (d) Schematic diagram showing optical bandgap modulation of solid graphene films at different annealing temperatures. The solid graphene films has an optical bandgap E_g of 2.20 eV , 1.78 eV , 0.77 eV and 0.67 eV when annealed at 500℃, 600℃,700 ℃ and 800℃ respectively.

ARTICLE

Intrinsic graphene has zero bandgap, which greatly limits its application, especially in the field of semiconductor. However, the energy bandgap of graphene can be opened up by either doping or controlling its size as demonstrated by others.[54-56] The graphene solution prepared using the liquid-phase catalysis method was spin-coated on to a substrate due to its good viscosity and then annealed at elevated temperature under vacuum to obtain solid-state graphene films, as shown in Fig. 3(a). Using the spin-coating deposition technique, it is possible to produce large area graphene film on any substrate because the size of the graphene film can be as large as the area of the substrate in this process. XPS measurements revealed the absence of iodine at the solid graphene film (see Fig. S3, ESI†), hence suggesting that the catalyst was removed upon annealing and there was no evidence of iodine doping. The graphene film was homogeneous and has a thickness of 609 nm as measured using AFM (as shown in Fig. 3(b)). Optical absorption characterization was performed on both the solution and the film during the preparation process. The absorption peaks of the GQDs solution were located at 285 nm during the nucleation stage. After the liquid-phase catalysis growth of graphene, the absorption peaks of the graphene solution red-shifted and were located at 353 nm. Moreover, its absorption spectrum was widened, which is a notable feature of graphene. After the annealing treatment, the liquid-phase graphene was solidified into graphene thin film, which led to a significant increase in its absorption intensity by at least three orders of magnitudes (e.g. 2015.9%) from that of the GQDs. A further widening of the absorption spectrum was observed (Fig. 3(c)), which can be attributed to the removal of moisture and carbon dioxide, thus resulting in a higher order of graphene films (see Fig. S4, ESI†). The optical bandgap of graphene can be calculated from its absorption spectrum since it is a direct bandgap material (see

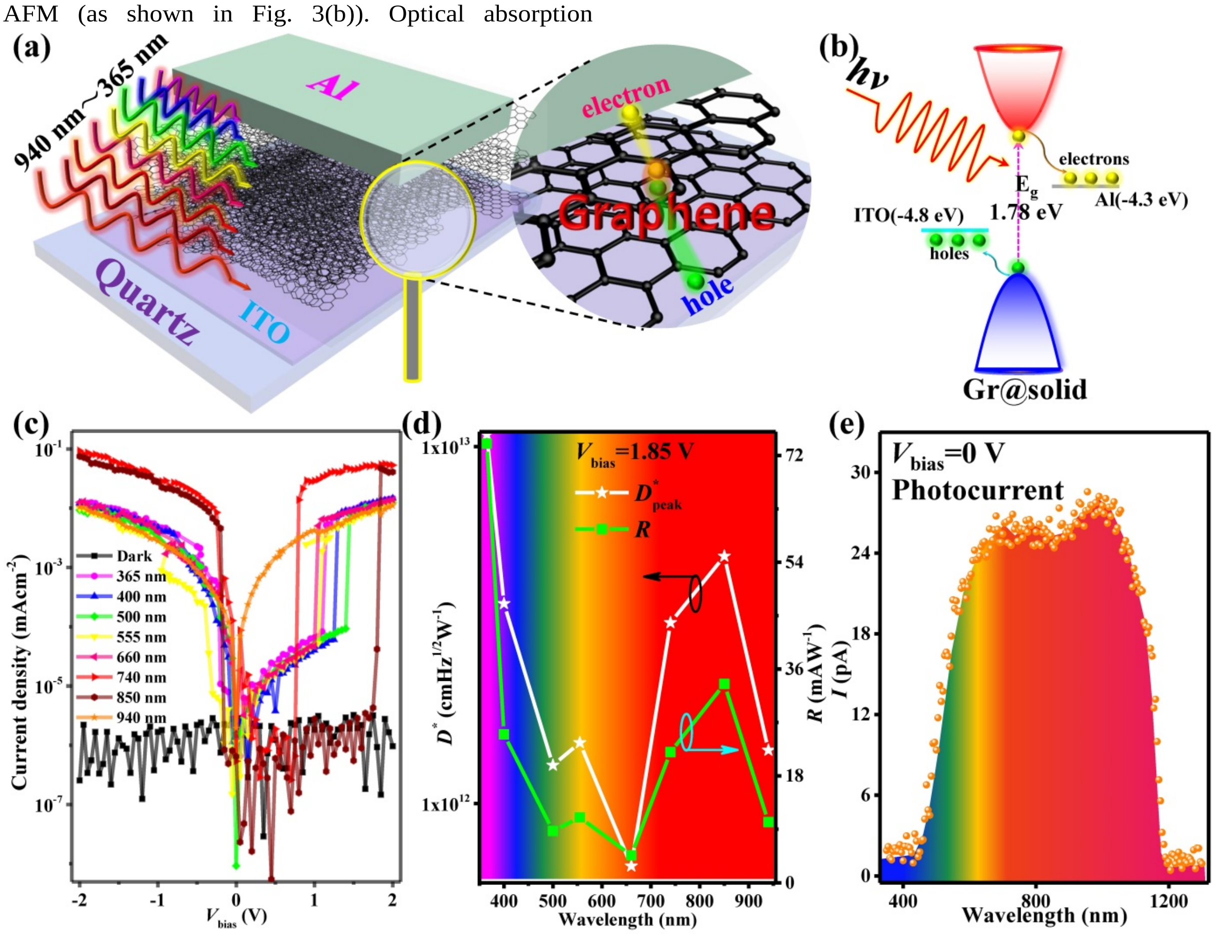

Fig. 4 Structure and characterization of a photodetector based on liquid-phase catalytic growth of graphene. (a) Schematic diagrams of the photodetector (left), and an enlarged diagram (right) of the active layer, which the exciton is produced by induced light and separated into electron and hole. (b) Energy band of the active layer consisting of the graphene film. (c) I-V characteristic of the photodetector under dark and illumination of LEDs with different wavelength ranging from 365 nm to 940 nm at various power density. (d) The peak detectivity and responsivity of photodetector with an applied voltage of 1.85 V at different wavelength. (e) The photocurrent spectrum of the photodetector without bias voltage, which has a broad response wavelength between 400 nm and 1200 nm.

Fig. S5 and Table S1, ESI†). Detailed calculation is shown in the Supplementary Discussion. The results showed that the bandgap of the solid graphene films varied significantly at different annealing temperatures, for example, the optical bandgap decreases with increasing annealing temperatures. Hence, the bandgap of liquid-phase catalytic graphene can be modulated by annealing treatment. The annealing temperature could influence the crystallinities of the solid graphene films, which contained stacking of graphene nanoflakes and incomplete carbon sources, therefore resulting in the bandgap modulation of the films. Based on the overall trend, the bandgap can be tuned from wide bandgap semiconductor (2.2 eV) at 500°C to conductor (0 eV) at sufficiently high temperature (see Fig. 3(d)). This is an exciting discovery as the graphene prepared by the liquid-phase catalysis method will lead to many novel applications in the semiconductor industry.

A simple photodetector structure, shown in Fig. 4(a), consisting of the graphene film as an absorbent layer was fabricated. The liquid-phase catalyzed graphene was spin-coated on the surface of ITO film. Fig. 4(a) illustrates the structure of the graphene films, which comprised of randomly stacked graphene flakes as the absorbent layer. The graphene film was then annealed at 600℃, which is limited by the maximum temperature of the ITO film.[46] An energy band structure of the photodetector with calculated optical bandgap of 1.78 eV is shown in Fig. 4(b). Fig. 4(c) shows *I-V* measurements performed on the photodetector under dark and illumination of LEDs with different wavelengths from 365 nm to 940 nm at various power densities (e.g. 365 nm @ 0.18 $mWcm^{-2}$, 400 nm @ 0.54 $mWcm^{-2}$, 500 nm @ 1.32 $mWcm^{-2}$, 555 nm @ 0.95 $mWcm^{-2}$, 660 nm @ 2.8 $mWcm^{-2}$, 740 nm @ 2.5 $mWcm^{-2}$, 850 nm @ 1.4 $mWcm^{-2}$, 940 nm @ 0.8 $mWcm^{-2}$). Such measurements demonstrated the capability of the photodetector in detecting wavelength ranging from ultraviolet to infrared. An important Fig. of merit for a photodetector[57] is responsivity (*R*), which can be calculated using the following:

$$R = J_{ph}/P_{opt} \quad (1)$$

where J_{ph} is photocurrent, which equals to absolute value of the current density under illumination subtracting that in the dark, and P_{opt} is incident optical power. Another important figure of merit is detectivity, D^*, which can be expressed as:

$$D^* = R/\sqrt{(2q|J_{dark}|)} \quad (2)$$

where J_{dark} is dark current density and q is unit charge. Using the *I–V* characteristics, both *R* and D^* can be calculated. Curves of *R* and D^* vs. applied voltage of the photodetector are shown in Fig. S6, ESI†. When applying 1.85 V, the photodetector exhibited peak detectivity D^*_{peak}) and responsivity as shown in Fig. 4(d). Under illumination at 365 nm, the detectivity and responsivity were increased to 1.1×10^{13} $cmHz^{1/2}W^{-1}$ and 81.3 mAW^{-1} respectively. Besides, the trend of D^* and *R* responding to wavelength was similar to that of photocurrent. As shown in Fig. 4(e), the photocurrent spectrum revealed a broad response wavelength of the photodetector, which ranged from 400 to 1200 nm. Such broad coverage in the visible and near-infrared range means that the graphene film is invaluable for applications in solar cell, photocatalysis and light-emitting diodes etc. Since the optical bandgap of the graphene film was 1.78 eV, its response wavelength should position at 696.6 nm (e.g. $\lambda_{peak}=1240(nm)/E_g$). The broad response wavelength therefore indicates extraordinary phenomena exhibited by the graphene film. Under the excitation of photons with specific energy, electron-hole pairs are excited inside the graphene. These electrons and holes are separated to Al and ITO electrodes respectively, as shown in Fig. 4(a). When photons with excessive energy (λ>365 nm) incident on to the graphene, heat (and/or other forms of energy) is also released, which contributes to the current of the photodetector.

Conclusions

Although the specific catalytic mechanism is still unclear, the liquid-phase catalytic growth of graphene has many significant differences comparing to current methods. Firstly, the growth process is safe and environment friendly. Besides, the method is facile and can produce high yield of graphene at room temperature. Furthermore, the solution based method allows easy and rapid production of graphene devices at very low cost. A possible growth mechanism could be the graphene quantum dots are rapidly catalysed to form graphene at room temperature due to the iodine atoms, which reduce the graphene growth barrier for the supplementary carbon source. Interestingly, the solid graphene film prepared using this method exhibited different characteristics as compared to conventional graphite, for example, the disordered stacking structure of graphene in the film can prevent electron coupling as observed in graphite, thus enhancing the absorption of graphene film. Importantly, the optical properties of the graphene film can be modified simply by controlling its annealing temperature. Due to ultralow absorption of graphene, the responsivity of graphene photodetectors is usually below 10 mAW^{-1}.[58,59] The detectivity of most graphene photodetectors is usually below 10^{12} $cmHz^{1/2}W^{-1}$ due to the commonly used planar device structure.[60,61] However, photodetector based on the graphene film exhibited excellent responsivity and detectivity of up to 81.3 mAW^{-1} and 1.1×10^{13} $cmHz^{1/2}W^{-1}$ respectively. The exceptional performances of the graphene film photodetector can attribute to two main factors; firstly the enhancement of absorption due to the disordered stacking of graphene within the film and secondly the vertical device structure, which can shorten the diffusion length of carriers. Finally, the broad response spectrum range of between 365 nm and 1200 nm is of paramount important to many applications in the field of optoelectronic, such as solar cell, light-emitting diode and photocatalysis etc.

Experimental

Synthesis of graphene by liquid-phase catalytic growth method.

Sucrose solution (0.1g/ml) was heated at 200℃ until it became brown solution. A precursor solution (0.5g/ml) was prepared by mixing the brown solution with alcohol and deionized water (at 3:1 ratio). Finally, iodine was added to the precursor solution at a mass ratio of 0.05:1. The sucrose and iodine were purchased from Chengdu Kelong Chemical Reagent Co. Ltd and Sinopharm Chemical Reagent Co. Ltd respectively.

Characterization of as-grown graphene and spin-coated graphene film.

UV-visible (U-4100) and TEM (Tecnai G2 TF30) characterization were performed on as-grown graphene and graphene film. The preparation process of graphene film for TEM measurement can be found in Supplementary Notes. Elementary composition of the graphene film were studied using XPS (X-ray photoelectron spectroscopy) (PHI VersaProbe II) with AlKα radiation. Uniformity and thickness of the graphene film was measured using Atomic Force Microscopy (AFM) (Seiko SPA-400).

Fabrication and characterization of photodetectors.
The liquid-phase graphene solution was spin-coated on a clear ITO at a rotary speed of 2500 rpm for 60 s. The graphene film was then annealed at 600℃ with temperature rising over a period of 30 min and kept constant for 60 min under a low pressure (<5.3 Pa) in a horizontal furnace. Next, aluminum electrode, acted as top electrode, was deposited on the solid graphene film by thermal evaporation under vacuum (～2.3×10^{-4} Pa). Gold wire was used to provide electrical connection to the cathode (Al) and anode (ITO). *J-V* measurements on the photodetector were performed using Keithley 2400 source meter. Photocurrent measurements from photodetector were carried out at zero bias voltage using spectral responsivity measurement system (DSR100-D30T75).

Author Contributions

Pin Tian performed the liquid-phase catalytic growth of graphene and prepared the photodetector. Shouzhang Yuan, Dengquan Yang, carried out the photoelectric response measurement and analyzed the data. Libin Tang, Jinzhong Xiang and Kar Seng Teng conceived the project. All authors participated in the discussion and contributed to the manuscript.

Conflicts of interest

There are no conflicts to declare.

Acknowledgements

This work was supported by National Natural Science Foundation of China [Grant No. 61106098, 51201150, 11374250 and 11864044], and the Key Project of Applied Basic Research of Yunnan Province, China [Grant No. 2012FA003].

Notes and references

1 K. S. Novoselov, A. K. Geim, S. V. Morozov, D. Jiang, Y. Zhang, S. V. Dubonos, I. V. Grigorieva and A. A. Firsov, *Science* 2004, **306**, 666-669.
2 T. Georgiou, R. Jalil, B. D. Belle, L. Britnell, R. V. Gorbachev, S. V. Morozov, Y.-J. Kim, A. Gholinia, S. J. Haigh, O. Makarovsky, L. Eaves, L. A. Ponomarenko, A. K. Geim, K. S. Novoselov and A. Mishchenko, *Nat. Nanotechnol.* 2013, **8**, 100-103.
3 D. Schurig, J. J. Mock, B. J. Justice, S. A. Cummer, J. B. Pendry, A. F. Starr and D. R. Smith, *Science* 2006, **314**, 977-980.
4 H. J. Park, J.-M. Jeong, S. G. Son, S. J. Kim, M. Lee, H. J. Kim, J. Jeong, S. Y. Hwang, J. Park, Y. Eom and B. G. Choi, *Adv. Funct. Mater.* 2021, **31**, 2011059.
5 H. Jang, Y. J. Park, X. Chen, T. Das, M.-S. Kim and J.-H. Ahn, *Adv. Mater.* 2016, **28**, 4184-4202.
6 Z. M. Tsikriteas, J. I. Roscow, C. R. Bowen and H. Khanbareh, *iScience* 2021, **24**, 101987.
7 S. H. Chae, W. J. Yu, J. J. Bae, D. L. Duong, D. Perello, H. Y. Jeong, Q. H. Ta, T. H. Ly, Q. A. Vu, M. Yun, X. Duan and Y. H. Lee, *Nat. Mater.* 2013, **12**, 403-409.
8 B. W. An, S. Heo, S. Ji, F. Bien and J. Park, *Nat. Commun.* 2018, **9**, 2458.
9 M. Malischewski, M. Adelhardt, J. Sutter, K. Meyer and K. Seppelt, *Science* 2016, **353**, 678-682.
10 J. H. Kang, S. Choi, Y. J. Park, J. S. Park, N. S. Cho, S. Cho, B. Walker, D. S. Choi, J.-W. Shin and J. H. Seo, *Carbon* 2021, **171**, 341-349.
11 I.-J. Park, T. I. Kim, T. Yoon, S. Kang, H. Cho, N. S. Cho, J.-I. Lee, T.-S. Kim and S.-Y. Choi, *Adv. Funct. Mater.* 2018, **28**, 1704435.
12 D.-W. Park, J. P. Ness, S. K. Brodnick, C. Esquibel, J. Novello, F. Atry, D.-H. Baek, H. Kim, J. Bong, K. I. Swanson, A. J. Suminski, K. J. Otto, R. Pashaie, J. C. Williams and Z. Ma, *ACS Nano* 2018, **12**, 148-157.
13 S. J. Lee, Y. R. Lim, S. Ji, S. K. Kim, Y. Yoon, W. Song, S. Myung, J. Lim, K.-S. An, J.-S. Park and S. S. Lee, *Carbon* 2018, **126**, 241-246.
14 X. T. Gan, R. J. Shiue, Y. D. Gao, I. Meric, T. F. Heinz, K. Shepard, J. Hone, S. Assefa and D. Englund, *Nat. Photonics* 2013, **7**, 883-887.
15 M. Massicotte, P. Schmidt, F. Vialla, K. G. Schadler, A. Reserbat-Plantey, K. Watanabe, T. Taniguchi, K. J. Tielrooij and F. H. L. Koppens, *Nat. Nanotechnol.* 2016, **11**, 42-46.
16 F. H. L. Koppens, T. Mueller, P. Avouris, A. C. Ferrari, M. S. Vitiello and M. Polini, *Nat. Nanotechnol.* 2014, **9**, 780-793.
17 Q. Qiu and Z. Huang, Adv. Mater. 2021, **33**, 2008126.
18 S. Chen, K. Jiang, Z. Lou, D. Chen and G. Shen, *Adv. Mater. Technol.* 2018, **3**, 1700248.
19 H. Kim and J. Ahn, *Carbon* 2017, **120**, 244-257.
20 H. Xu, Y. F. Lu, J. X. Xiang, M. K. Zhang, Y. J. Zhao, Z. Y. Xie and Z. Z. Gu, *Nanoscale* 2018, **10**, 2090-2098.
21 R. R. Nair, P. Blake, A. N. Grigorenko, K. S. Novoselov, T. J. Booth, T. Stauber, N. M. R. Peres and A. K. Geim, *Science* 2008, **320**, 1308.
22 K. I. Bolotin, K. J. Sikes, Z. Jiang, M. Klima, G. Fudenberg, J. Hone, P. Kim and H. L. Stormer, *Solid State Commun.* 2008, **146**, 351-355.
23 A. A. Balandin, S. Ghosh, W. Z. Bao, I. Calizo, D. Teweldebrhan, F. Miao and C. N. Lau, *Nano Lett.* 2008, **8**, 902-907.
24 K. G. Zhou, K. S. Vasu, C. T. Cherian, M. Neek-Amal, J. C. Zhang, H. Ghorbanfekr-Kalashami, K. Huang, O. P. Marshall, V. G. Kravets, J. Abraham, Y. Su, A. N. Grigorenko, A. Pratt, A. K. Geim, F. M. Peeters, K. S. Novoselov and R. R. Nair, *Nature* 2018, **559**, 236-240.
25 S. P. Singh, Y. Li, J. Zhang, J. M. Tour and C. J. Arnusch, *ACS Nano* 2018, **12**, 289-297.
26 H. T. Sun, L. Mei, J. F. Liang, Z. P. Zhao, C. Lee, H. L. Fei, M. N. Ding, J. Lau, M. F. Li, C. Wang, X. Xu, G. L. Hao, B. Papandrea, I. Shakir, B. Dunn, Y. Huang and X. F. Duan, *Science* 2017, **356**, 599-604.
27 L. Fornasini, S. Scaravonati, G. Magnani, A. Morenghi, M. Sidoli, D. Bersani, G. Bertoni, L. Aversa, R. Verucchi, M. Ricco, P. P. Lottici and D. Pontiroli, *Carbon* 2021, **176**, 296-306.
28 C. W. Park, J.-H. Lee, J. K. Seo, W. Y. Jo, D. Whang, S. M. Hwang and Y.-J. Kim, *Nat. Commun.* 2021, **12**, 2145.
29 F. Bonaccorso, L. Colombo, G. H. Yu, M. Stoller, V. Tozzini, A. C. Ferrari, R. S. Ruoff and V. Pellegrini, *Science* 2015, **347**, 1246501.
30 H. L. Wang, Y. Yang, Y. Y. Liang, J. T. Robinson, Y. G. Li, A. Jackson, Y. Cui and H. J. Dai, *Nano Lett.* 2011, **11**, 2644-2647.
31 J. J. Chen, J. Meng, Y. B. Zhou, H. C. Wu, Y. Q. Bie, Z. M. Liao and D. P. Yu, *Nat. Commun.* 2013, **4**, 1921.
32 L. J. Yi, T. C. Chang, Feng, Y. Y. Zhang, J. Wang and B. Huang, *Carbon* 2017, **118**, 348-357.
33 A. Reina, X. T. Jia, J. Ho, D. Nezich, H. B. Son, V. Bulovic, M. S. Dresselhaus and J. Kong, *Nano Lett.* 2009, **9**, 30-35.
34 X. S. Li, W. W. Cai, J. H. An, S. Kim, J. Nah, D. X. Yang, R. Piner, A. Velamakanni, I. Jung, E. Tutuc, S. K. Banerjee, L. Colombo and R. S. Ruoff, *Science* 2009, **324**, 1312-1314.
35 E. Lee, S. G. Lee, H. C. Lee, M. Jo, M. S. Yoo and K. Cho, *Adv. Mater.* 2018, **30**, 1706569.
36 B. W. Li, D. Luo, L. Zhu, X. Zhang, S. Jin, M. Huang, F. Ding and R. S. Ruoff, *Adv. Mater.* 2018, **30**, 1706504.
37 S. Subramanian, D. D. Deng, K. Xu, N. Simonson, K. Wang, K. H. Zhang and J. Li, *Carbon* 2017, **125**, 551-556.

38 K. V. Emtsev, A. Bostwick, K. Horn, J. Jobst, G. L. Kellogg, L. Ley,; J. L. McChesney, T. Ohta, S. A. Reshanov, J. Rohrl, E. Rotenberg, A. K. Schmid, D. Waldmann, H. B. Weber and T. Seyller, *Nat. Mater.* 2009, **8**, 203-207.
39 S. Mukherjee, N. Nateghi, R. M. Jacobberger, E. Bouthillier, M. de la Mata, J. Arbiol, T. Coenen, D. Cardinal, P. Levesque, P. Desjardins, R. Martel, M. S. Arnold and O. Moutanabbir, *Adv. Funct. Mater.* 2018, **28**, 1705592.
40 C. H. Chen, C. T. Lin, Y. H. Lee, K. K. Liu, C. Y. Su, W. J. Zhang and L. J. Li, *Small* 2012, **8**, 43-46.
41 S. Ravula, S. N. Baker, G. Kamath and G. A. Baker, *Nanoscale* 2015, **7**, 4338–4353.
42 L. H. Tang, Y. Wang, Y. M. Li, H. B. Feng, J. Lu and J. H. Li, *Adv. Funct. Mater.* 2009, **19**, 2782-2789.
43 J. M. Cai, P. Ruffieux, R. Jaafar, M. Bieri, T. Braun, S. Blankenburg, M. Muoth, A. P. Seitsonen, M. Saleh, X. L. Feng, K. Mullen and R. Fasel, *Nature* 2010, **466**, 470-473.
44 R. Denk, M. Hohage, P. Zeppenfeld, J. M. Cai, C. A. Pignedoli, H. Sode, R. Fasel, X. L. Feng, K. Mullen, S. D. Wang, D. Prezzi, A. Ferretti, A. Ruini, E. Molinari and P. Ruffieux, *Nat. Commun.* 2014, **5**, 4253.
45 L. B. Tang, X. M. Li, R. B. Ji, K. S. Teng, G. Tai, J. Ye, C. S. Wei and S. P. Lau, *J. Mater. Chem.* 2012, **22**, 5676.
46 S. K. Lai, L. Tang, Y. Y. Hui, C. M. Luk and S. P. Lau, *J. Mater. Chem. C.* 2014, **2**, 6971-6977.
47 Q. Wu, J. Lee, J. Sun and Y. J. Song, *Carbon* 2018, **138**, 76-80.
48 J. Kim, H. Sakakita and H. Itagaki, *Nano Lett.* 2019, **19**, 739−746.
49 Z. Bo, Y. Yang, J. H. Chen, K. H. Yu, J. H. Yan and K. F. Cen, *Nanoscale* 2013, **5**, 5180-5204.
50 A. Narita, X.-Y. Wang, X. Feng and K. Müllen, *Chem. Soc. Rev*. 2015, **44**, 6616-6643.
51 F. R. Fischer, *Adv. Polym. Sci.* 2017, **278**, 33-66.
52 V. P. Pham, H. S. Jang, D. Whang and J. Y. Choi, *Chem. Soc. Rev.* 2017, **46**, 6276-6300.
53 R. Matassa, S. Orlanducci, E. Tamburri, V. Guglielmotti, D. Sordi, M. L. Terranova, D. Passeri and M. Rossi, *J. Appl. Crystallogr.* 2014, **47**, 222-227.
54 W. Xu, L. Wang, Y. Liu, S. Thomas, H. K. Seo, K. I. Kim, K. S. Kim and T. W. Lee, *Adv. Mater.* 2015, **27**, 1619–1623.
55 X. Z. Xu, C. Liu, Z. H. Sun, T. Cao, Z. H. Zhang, E. G. Wang, Z. F. Liu and K. H. Liu, *Chem. Soc. Rev.* 2018, **47**, 3059-3099.
56 F. P. Ouyang, S. L. Peng, Z. X. Yang, Y. Chen, H. Zou and X. Xiong, *Phys. Chem. Chem. Phys.* 2014, **16**, 20524-20531.
57 X. Gong, M. H. Tong, Y. J. Xia, W. Z. Cai, J. S. Moon, Y. Cao, G. Yu, C. L. Shieh, B. Nilsson and A. J. Heeger, *Science* 2009, **325**, 1665-1667.
58 J. F. Li, C. Zhao, B. Y. Liu, C. Y. You, F. H. Chu, N. Tian, Y. F. Chen, S. Y. Li, B. X. An, A. J. Cui, X. P. Zhang, H. Yan, D. M. Liu and Y. Z. Zhang, *Appl. Surf. Sci.* 2019, **473**, 633–640.
59 C.-H. Liu, Y.-C. Chang, T. B. Norris and Z. Zhong, *Nat. Nanotechnol.* 2014, **9**, 273-278.
60 P. Tian, L. Tang, K. S. Teng, J. Xiang and S. P. Lau, *Adv. Mater. Technol.* 2019, **4**, 1900007.
61 G. Wang, M. Zhang, D. Chen, Q. L. Guo, X. F. Feng, T. C. Niu, X. S. Liu, A. Li, J. W. Lai, D. Sun, Z. M. Liao, Y. Q. Wang, P. K. Chu, F. Q. Ding, X. M. Xie, Z. F. Di and X. Wang, Nat. Commun. 2018, **9**, 5168.

